Understanding the importance of Cu(I) intermediates in self-reducing molecular inks for flexible electronics

Wouter Marchal[1,5*], Alessandro Longo[2,3], Valérie Briois[4], Kristof Van Hecke[5], Ken Elen[1,6], Marlies K. Van Bael[1,6], An Hardy[1,6]

[1] UHasselt – Hasselt University, Institute for Materials Research (IMO-IMOMEC), Inorganic and Physical Chemistry, Agoralaan building D, 3950 Diepenbeek, Belgium
[2] European Synchrotron Radiation Facility, CS40220, Avenue des Martyrs 71, 38043 Grenoble Cedex 9, France
[3] UOS Palermo, CNR, ISMN, via Ugo La Malfa 153, 90146 Palermo, Italy
[4] Synchrotron SOLEIL, UR1-CNRS, L'Orme des Merisiers, Saint-Aubin, BP 48, 91192 Gif-Sur-Yvette Cedex, France
[5] XStruct, Ghent University, Department of Chemistry, Krijgslaan 281-S3, 9000 Ghent, Belgium
[6] Imec vzw, Division IMOMEC, Agoralaan building D, 3590 Diepenbeek, Belgium
* corresponding author

Supporting information

S1: overview of the decision making process to identify the number of components in the in-situ reduction of $Cu(hex)_2(HCOO)_2$ after performing the principal component analysis algorithm. The trajectory shape of the scores for each component as a function of reaction coordinates (figure S1.1) are presented together with their eigenvalues. In addition the 2D trajectory analysis of the scores and plots showing the variance and eigenvalues against the component number are helpful to determine the amount of components which incorporate structural information.
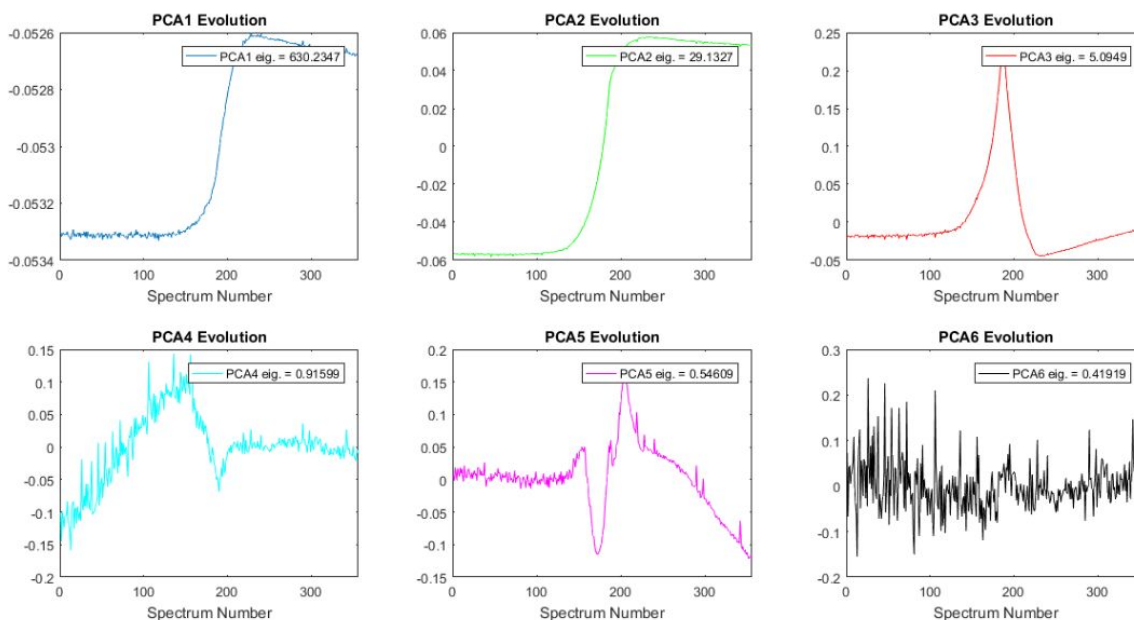
Figure S1.1: Overview of the scores for the first six eigenvectors as a function of reaction coordinates. Whereas component 6 mainly consists of high frequency noise, the first 3 components clearly contain systematic features which contribute to the total variance in the data matrix. Component 4 and 5 seem to be composed of some structural information together with noise. Judging by the associated eigenvalues, the first 3 components are definitely to be included, whereas the component 4 and 5 are connected to a quite small eigenvalue. Scree plot representation of the eigenvalues (figure S1.2) is instructive to assess this more clearly.
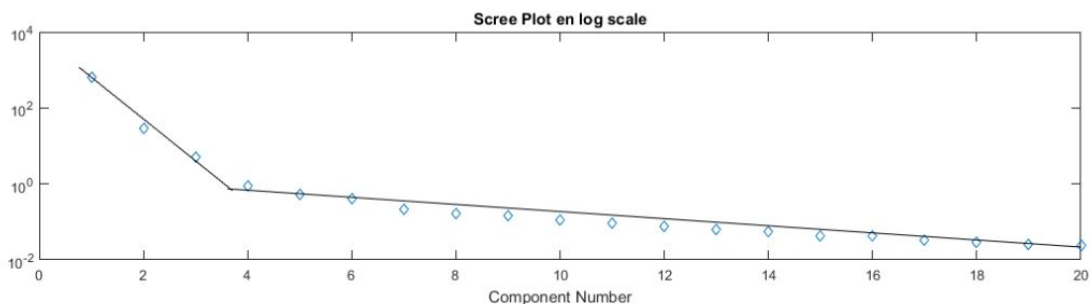

Figure S1.2: Scree plot showing the ranked eigenvalues against the component number. A clear break in the slope can be observed between component 3 and 4, suggesting the three first components include the large majority of the total variance, and the higher components are explained by noise and systematic error.
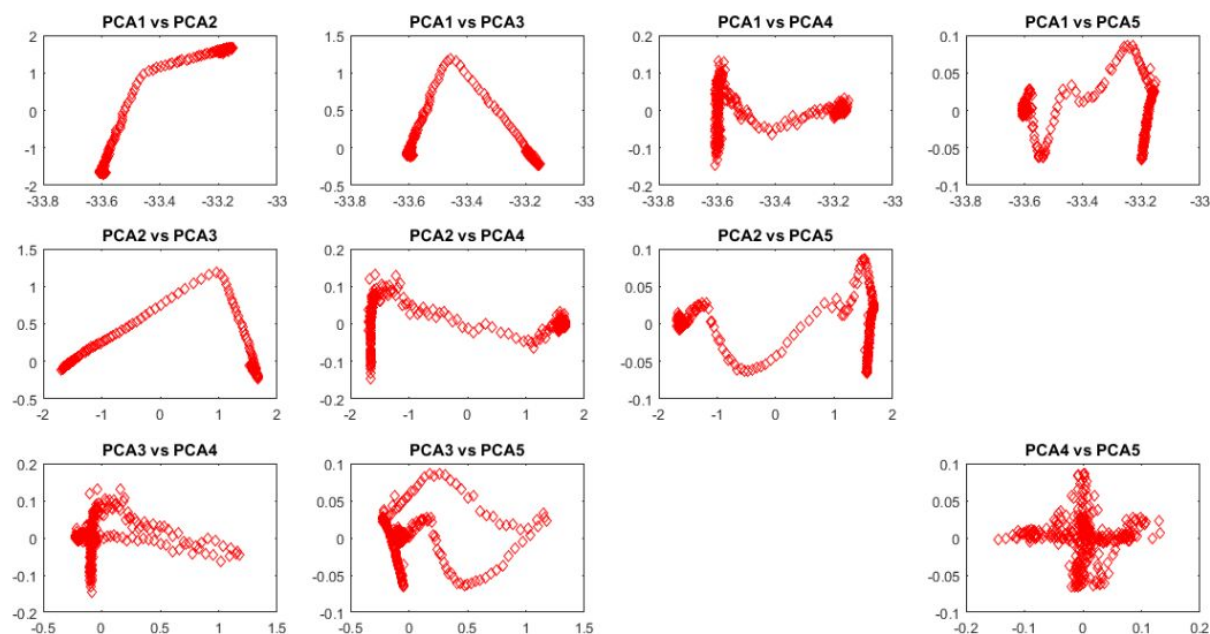
Figure S1.3: 2D trajectory plots of scores as a function of each separate principal component show that mainly the PCA1 vs PCA2, the PCA1 vs PCA3 and PCA2 vs PCA3 exhibit a large degree of systematisms. Note the difference in y-axis scale between these 3 plots and all other PCA 2D representations.
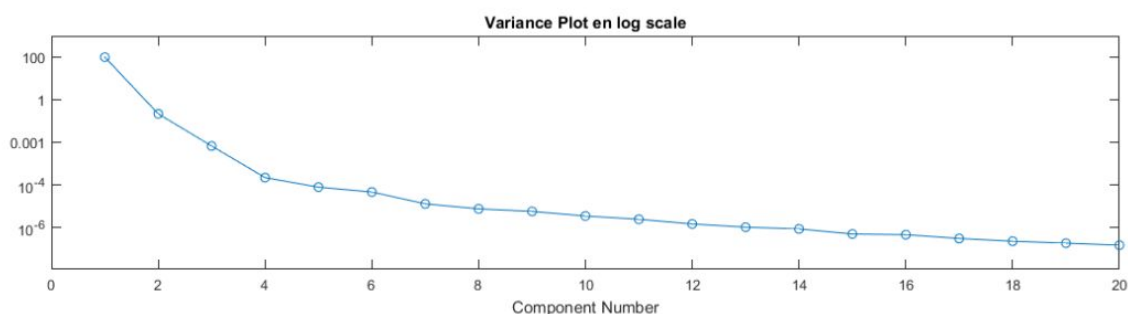

Figure S1.4: Ordering of the components according to the percentage of explained variance. Also here, a break between the 3rd and 4th component can be observed. Considering all evidences together, the decision to use 3 components for the data reconstruction with MCR-ALS can be rationalized.

S2: TG-MS analysis of the $Cu(hex)_2(HCOO)_2$ MOD ink dried at 60 °C and in vacuum (RT). The measurement is carried out in N_2 atmosphere with a 5°C/min heating rate. The graph illustrates the evaporation of a little ethanol (mainly m/z = 45, 44, 30, 18 and 16) around 70 °C and the *in-situ* reduction (around 100 -135 °C). The Cu(II)→ Cu(I) →Cu(0) sequence is not completely resolved but the figure allows to observe a shoulder in the CO_2 evolution profile (m/z = 44). The maximum of the hexylamine evolution is clearly positioned at slightly higher temperatures (m/z = 101, 69, 56,…). The gray vertical lines denote the maxima of the CO_2 peak (m/z = 44) and the hexylamine parent ion peak (m/z = 101). Also the H_2 signal (m/z = 2) suggests a stepwise decomposition profile.
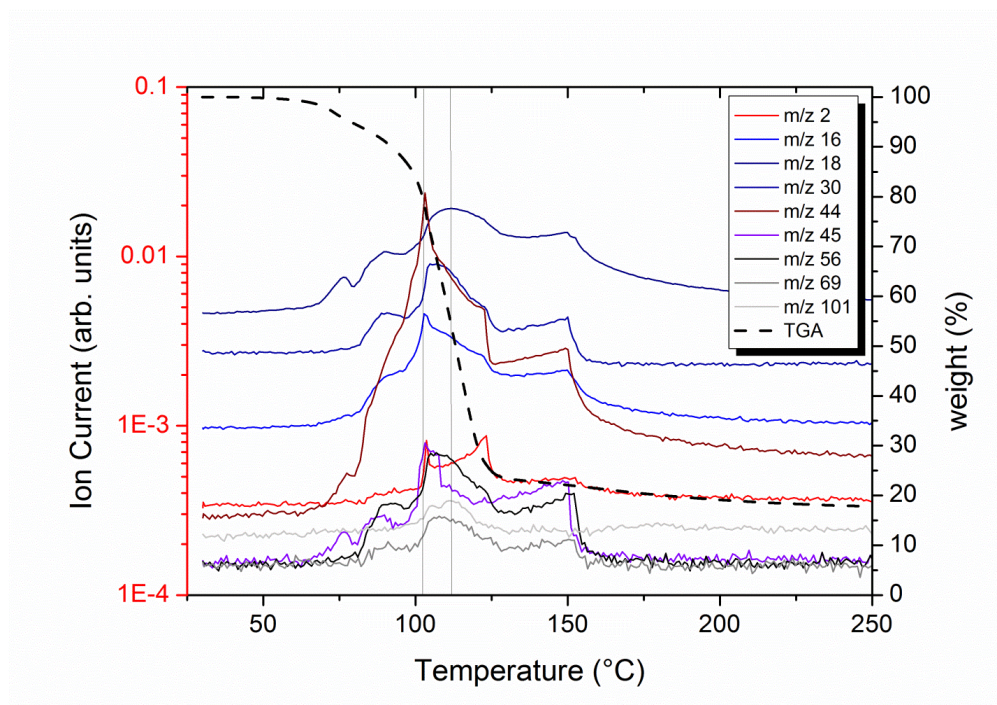
S3

Figure S2: Thermogram of 4 mg of the Cu(hex)$_2$(HCOO)$_2$ complex. The black dashed line is the corresponding thermogravimetric profile (right Y axis), the colored solid lines describe ion currents corresponding to the electron ionization of the evolving gasses. The vertical lines emphasize the maximum of the carbon dioxide(103 °C) and the hexylamine mother nuclide (111 °C) profile. Typical m/z ratio's for the formate reduction include 44 and 2 (H$_2$), whereas hexylamine can be identified considering m/z = 101, 69, 56, 45, 30 and 18.

S3: the TG-FTIR Gram-Schmidt integration curves of Cu(hex)$_2$(HCOO)$_2$ clearly shows that the CO$_2$ evolution onset takes place earlier compared to the hexylamine evolution. In addition a clear shoulder in the CO$_2$ is observed after the maximum intensity GS, suggesting the stepwise reduction mechanism. The evolution of small residual portions of ethanol (the solvent in the MOD ink synthesis) before the in-situ reduction mechanism can also be confirmed.
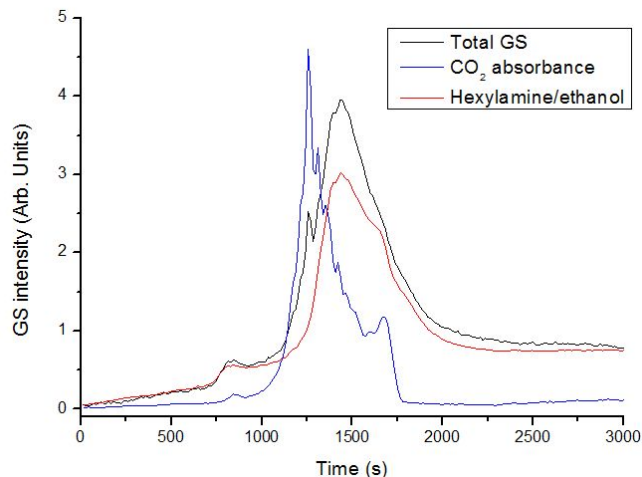
Figure S3: Gram-Schmidt profiles of the integrated CO_2 signal (2400-2250 cm^{-1}) and the CH_3-CH_2 stretching signal (hexylamine) as a function of measurement time. The conversion to effective sample temperature can be made considering the starting temperature (25 °C), the heating rate (5°C/min) and the ΔT between the furnace and sample thermocouple readout (approx. 20 °C).

S4: TG-DSC measurement of a Cu(etam)$_2$(HCOO)$_2$ complex, heated in nitrogen at 5 °C/min, together with the ion currents of the evolved gasses, detected via mass spectrometry. The complex is dried at 80 °C prior analysis to remove the ethanol excess. The presence of different consecutive steps is clearly observed in the DSC curve (exothermic and endothermic peak during major weight loss) and via analysis of the different mass fragments: H2O and CO2 (m/z 17, 18 and 44) evolve earlier compared to the characteristic fragments of ethanolamine (m/z: 61,43, 42, 30, 26,…)

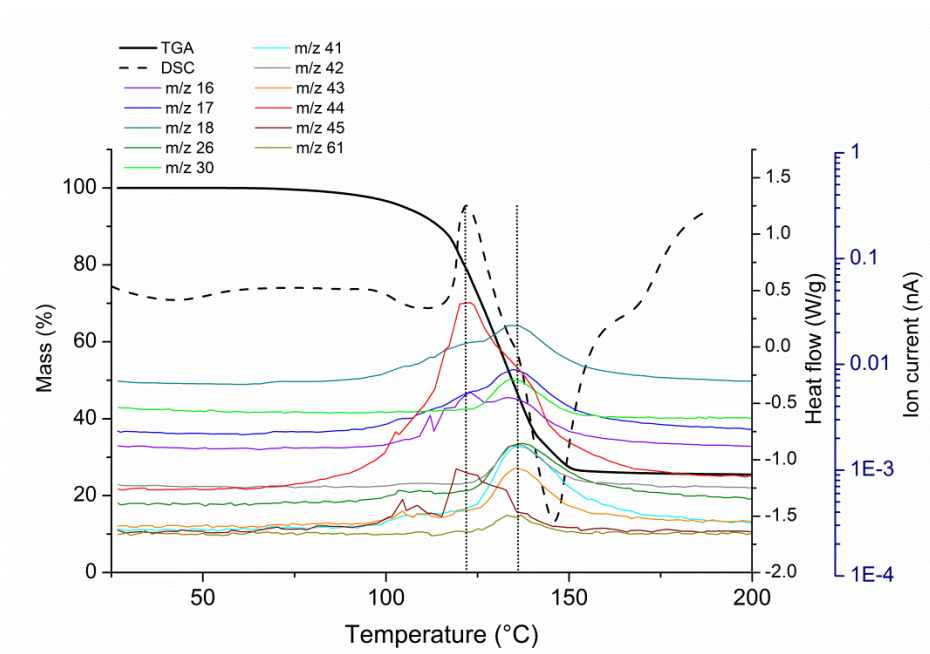*Figure S4: Thermogram and evolved gas analysis of Cu(etam)$_2$(HCOO)$_2$. The black dashed line is the corresponding DSC profile (right Y axis), the solid black line corresponds to the mass loss profile (left Y axis). The colored solid lines(second right Y-axis) describe the ion currents corresponding to the electron ionization of the evolving gasses. The blue vertical lines emphasize the maximum of the carbon dioxide(129 °C) and the ethanolamine parent ion (145 °C) profile.*

S5: Cyclic voltammetry experiments, carried out in an electrochemical cell depicted on the right hand side, show that amine coordination significantly shifts the cathodic copper reduction potential. A film of different copper complexes is drop casted on a Pt wafer which is connected to a Cu disk to serve as the working electrode. The cathodic reduction potential is extracted from the voltammograms. The copper reduction in the studied potential window is evidenced by a picture of the copper deposition on the Pt working electrode wafer after cycling. The absolute values of the current are of subordinate importance as the thickness of the deposition on the working electrode was not controlled.
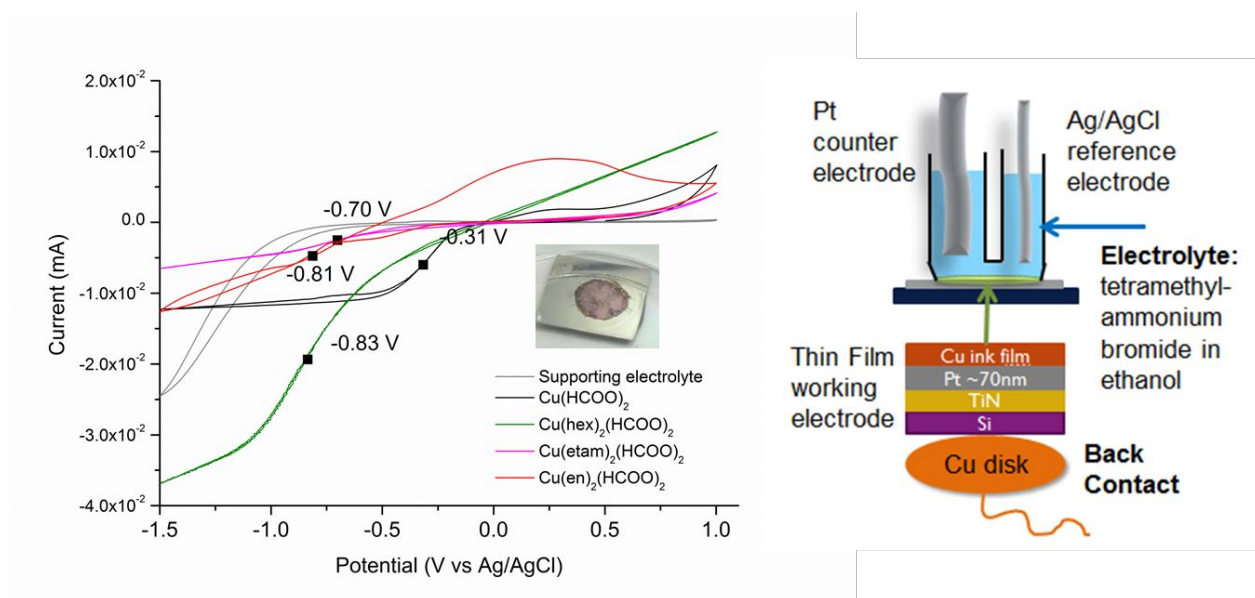

Figure S5: CV scans (50 mV/s and 10 mV/s) of different Cu-complexes, showing a lower reduction potential upon amine coordination. The cell geometry is presented on the right side, emphasizing the separation between the different electrodes. A platinum grid counter and Ag/AgCl reference electrode were used in a solution of tetramethylammoniumbromide (0.2 M) in ethanol as the supporting electrolyte.

S6: EXAFS structure determination of the synthesized copper complexes. The fitting is performed in k-space with k^3 weighting, whereupon the spectra and models are Fourier transformed to R-space. The fitted parameters are the distances r(Å) and the Debye-Waller factor σ^2 (Å^2). The original E$_0$ value is

determined as the maximum of the first XANES derivative peak, and E_0 shifts between 7.5 ± 2.0 eV were observed in all fittings. All fits obey the Nyquist criterion[1] and R^2 lack of fit values are reported.
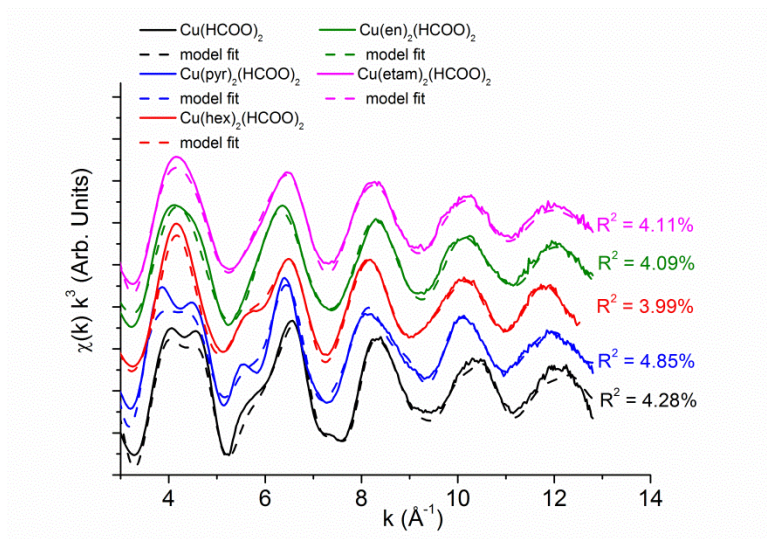

Figure S6.1: k-space fittings of the reported copper(II)-amine-formato complexes and their respective lack of fit values.
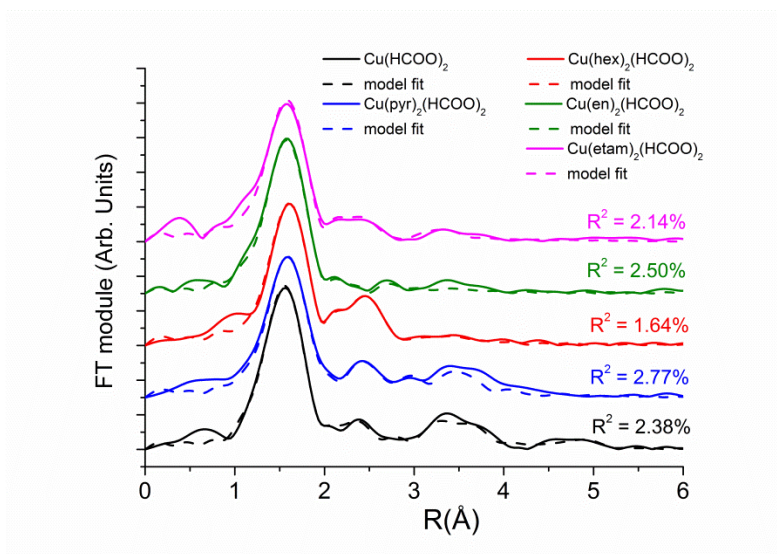

Figure S6.2: R-space fittings of the reported Cu(II)-amine-formato complexes and their respective lack of fit values.

Table S6.1: overview of the fitted parameters for the Cu(HCOO)$_2$ model structure, including a random multiple scattering (MS) shell to account for the substantial contribution of the higher shells which could not be included explicitly in the model given the limited independent degrees of freedom that can be fitted (Nyquist criterion). The table shows the degeneracy (N), distance (r), Debye-Waller factor (σ^2), a 95 % confidence interval for the distance based on r-E_0 shift mapping and the physical meaning of the shell. The fitted E_0 shift was found to be 7.31 eV.

S7

shell	degeneracy	r fit	σ² fit	r 95 % CI	Meaning
1	4	1.95	0.006	1.94 - 1.97	4 O's in pyramidal base, SS
2	1	2.29	0.013	2.17 - 2.40	1 O top tetragonal pyramid, SS
3	4	2.81	0.011	2.75 - 2.87	4 C's of formate connected to shell 1 O's, SS
4	8	3.03	0.006	2.90 - 3.14	Cu-O-C, pyramid base, MS
5	1	3.40	0.013	3.30 - 3.50	Cu-Cu distance 1, SS
6	8	3.91	0.006	-	Cu-O-O, Cu-O-Cu-O, pyramid base, MS
7	x = 6.74	4.15	0.009	4.10 - 4.21	random MS contribution, derived from feff file
8	2	5.03	0.014	4.88 - 5.17	Cu-Cu distance: 5.04 in crystal str, SS
9	2	5.12	0.011	5.06 - 5.29	Cu-Cu distance : 4.625 in crystal str, SS

Table S6.2: overview of the fitted parameters for the Cu(pyr)$_2$(HCOO)$_2$ model structure, including a random multiple scattering (MS) shell to account for the substantial contribution of the higher shells (especially due to the pyridine MS pathways) which could not be included explicitly in the model given the limited independent degrees of freedom that can be fitted (Nyquist criterion). The table shows the degeneracy (N), distance (r), Debye-Waller factor (σ²), a 95 % confidence interval for the distance based on r-E$_0$ shift mapping and the physical meaning of the shell. The fitted E$_0$ shift was found to be 7.58 eV.

Shells	degeneracy	r fit	σ² fit	r 95 % CI	Meaning
1	2	1.97	0.015	1.92 - 2.02	Cu-O bridging formate equatorial SS
2	2	2.00	0.002	1.99 - 2.02	Cu-N pyridine axial SS
3	1	2.44	0.005	2.39 - 2.49	Cu-O monodentate formate, equatorial SS
4	2	2.70	0.004	2.66 - 2.75	Cu-C formate SS
5	4	2.91	0.004	2.88 - 2.93	Cu-C pyridine SS
6	8	3.27	0.006	3.14 - 3.40	Cu-N-C en Cu-C-N MS pyridine
7	4	3.94	0.015	-	O-Cu-O and Cu-O-Cu-O linear MS
8	4	4.00	0.002	-	N-Cu-N and Cu-N-Cu-N linear MS
9	x = 22.98	4.20	0.016	4.13 - 4.26	mixed MS contribution pyridine rings

Table S6.3: overview of the fitted parameters for the Cu(en)$_2$(HCOO)$_2$ model structure. The table shows the degeneracy (N), distance (r), Debye-Waller factor (σ²), a 95 % confidence interval for the distance based on r-E$_0$ shift mapping and the physical meaning of the shell. The fitted E$_0$ shift was found to be 8.87 eV.

shell	degeneracy	r fit	σ² fit	r 95 % CI	Meaning
1	4	2.02	0.005	2.01 -2.03	4 equatorial N's, en, SS
2	2	2.70	0.017	2.65 -2.74	2 axial O's, formate, SS
3	4	2.88	0.007	2.86 -2.90	4 equivalent C's, en, SS
4	2	3.42	0.005	3.37 -3.46	Cu-C, formate, SS
5	2	3.59	0.005	3.55 -3.62	Cu-O, other O formate, SS

6	2	3.76	0.003	3.72 -3.79	Cu-O other scattering center, SS
7	8	4.04	0.005	-	N-Cu-N, N-Cu-N-Cu, en, MS

Table S6.4: overview of the fitted parameters for the $Cu(hex)_2(HCOO)_2$ model structure. The table shows the degeneracy (N), distance (r), Debye-Waller factor (σ^2), a 95 % confidence interval for the distance based on r-E_0 shift mapping and the physical meaning of the shell. The fitted E_0 shift was found to be 5.91 eV.

Shell	degeneracy	r fit	σ^2 fit	r 95 % CI	Meaning
1	2	1.94	0.007	constr.	Cu-N, equatorial, hexylamine, SS
2	2	1.99	0.003	1.98-1.99	Cu-O, equatorial, formate, SS
3	2	2.51	0.012	2.48-2.54	Cu-O, ineq. axial, formate, SS
4	2	2.70	0.003	2.69-2.71	Cu-C, hexylamine, SS
5	2	2.87	0.005	2.84-2.90	Cu-C, formate, SS
6	4	3.20	0.004	constr.	Cu-O-C, formate (equatorial O), MS
7	4	3.88	0.007	-	Cu-N-(Cu)-N, hexylamine, MS
8	4	3.97	0.003	-	Cu-O-(Cu)-O, equatorial O, formate, MS

Table S6.5: overview of the fitted parameters for the $Cu(etam)_2(HCOO)_2$ model structure. The table shows the degeneracy (N), distance (r), Debye-Waller factor (σ^2), a 95 % confidence interval for the distance based on r-E_0 shift mapping and the physical meaning of the shell. The fitted E_0 shift was found to be 5.71 eV.

shell	degeneracy	r fit	σ^2 fit	r 95% CI	Meaning
1	2	1.94	0.012	constr.	Cu-N, equatorial, ethanolamine, SS
2	2	1.98	0.003	1.97 - 1.99	Cu-O, equatorial, monodentate formate, SS
3	2	2.43	0.008	2.41 - 2.46	Cu-O, axial, OH-ethanolamine, SS
4	2	2.65	0.002	2.63 - 2.66	Cu-C, formate, monodentate, SS
5	4	2.81	0.007	2.79 - 2.83	Cu-C, 4 equivalent C's, ea, bidentate, SS
6	2	3.29	0.012	3.22 - 3.35	Cu-O, other O monodentate formate, SS
7	4	3.88	0.012	-	Cu-N-N, Cu-N-Cu-N, ea, MS
8	4	3.95	0.003	-	Cu-O-O, CuO-Cu-O, formate, MS

S7: overview of the thermal decomposition profiles of the studied copper complexes. The differential thermogravimetric (DTG) analysis maxima are highlighted on the thermograms. For both the $Cu(hex)_2(HCOO)_2$ and $Cu(etam)_2(HCOO)_2$ complexes, determination of a single maximum in the DTG is not straightforward and therefore a region of maximum decomposition is shown. For the $Cu(pyr)_2(HCOO)_2$ complex, the evolution of 1 pyridine equivalent is observed well before the *in-situ* reduction. Apart from the mass ratio, the pre-reduction loss of a single pyridine causing the formation of $Cu(pyr)(HCOO)_2$ can be evidenced by evolved gas analysis (supporting info S13).
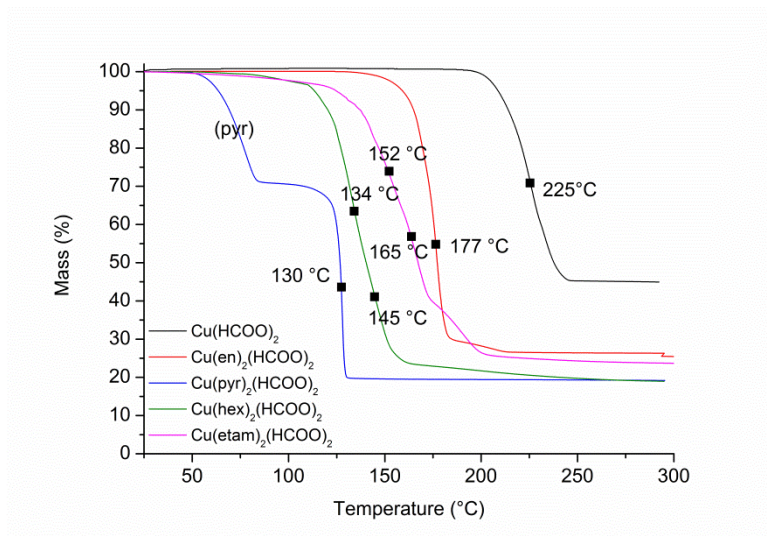
Figure S7: Thermogravimetric analysis of the investigated copper complexes using a heating rate of 10 °C/min in nitrogen atmosphere, emphasizing the maxima of their respective derivatives.

S8: the derivative XANES spectra for the $Cu(hex)_2(HCOO)_2$, $Cu(etam)_2(HCOO)_2$ and $Cu(en)_2(HCOO)_2$ complexes consist out of two distinct maxima, typical of distorted octahedral coordination environments according to *Frenkel et al.[2]*. Moreover, the peak separation between B and C is quite large (6.0 eV - etam, 6.6 eV - hex and 6.8 eV - en respectively), suggesting strong tetragonally distorted octahedra. This corresponds to the values found in the EXAFS fitting (S5).
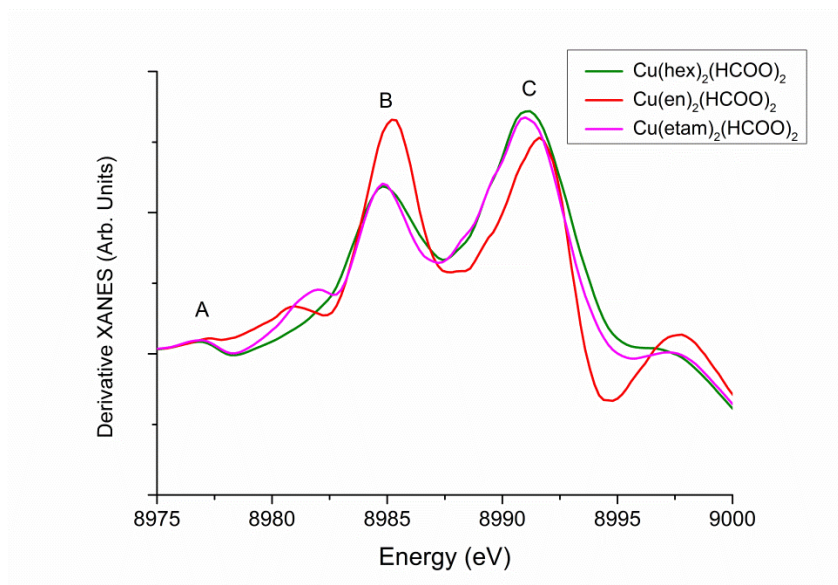

Figure S8: Derivative XANES spectra of the tetragonally distorted octahedral complexes. Signal A corresponds to the pre-edge feature of the spin forbidden 1s->3d transition, whereas the separation between B and C contains information on the magnitude of the tetragonal distortion .It can be concluded

S10

that the Cu(etam)$_2$(HCOO)$_2$ complex exhibits a tetrahedral distortion which is less pronounced. This result corresponds with the found first shell distances via EXAFS fitting (SI 6)

S9: In-situ XAS measurement dataset (top) of the Cu(etam)$_2$(HCOO)$_2$ complex, showing the stepwise transition from Cu(II) to Cu(I), starting around 100 °C, and from Cu(I) to Cu(0). The Cu(I) species can be clearly recognized due to its distinct pre-edge features. After applying the PCA-MCR-ALS algorithm, the pure components (left) and their respective concentration profiles can be isolated, confirming the trends observed in the full data matrix.
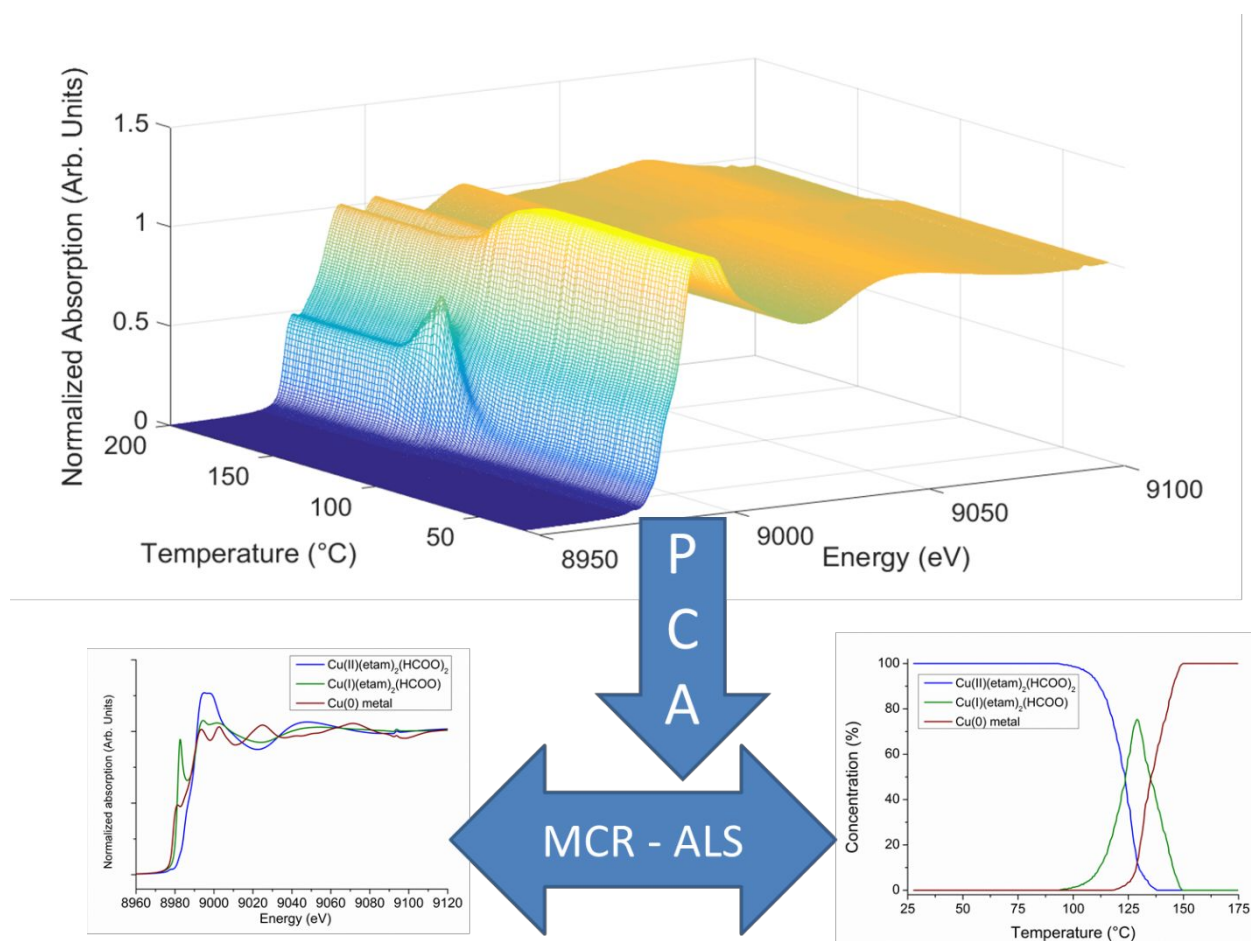

Figure S9.1: In-situ XAS measurements of a Cu(etam)$_2$(HCOO)$_2$ sample, heated from room temperature up to 200 °C (5 °C/min) in He atmosphere (showing 1 spectrum out of 3). The data reduction is performed as described in the experimental section.

S10: illustration of the ability to reconstruct the original dataset by multiplication of the 'pure' copper spectra determined by MCR-ALS analysis, with their respective concentration profiles as shown in figure 4. Both the original data and (figure S10.1) and the reconstruction together with the residuals (difference between the original and reconstructed data points, figure S10.2) are given.
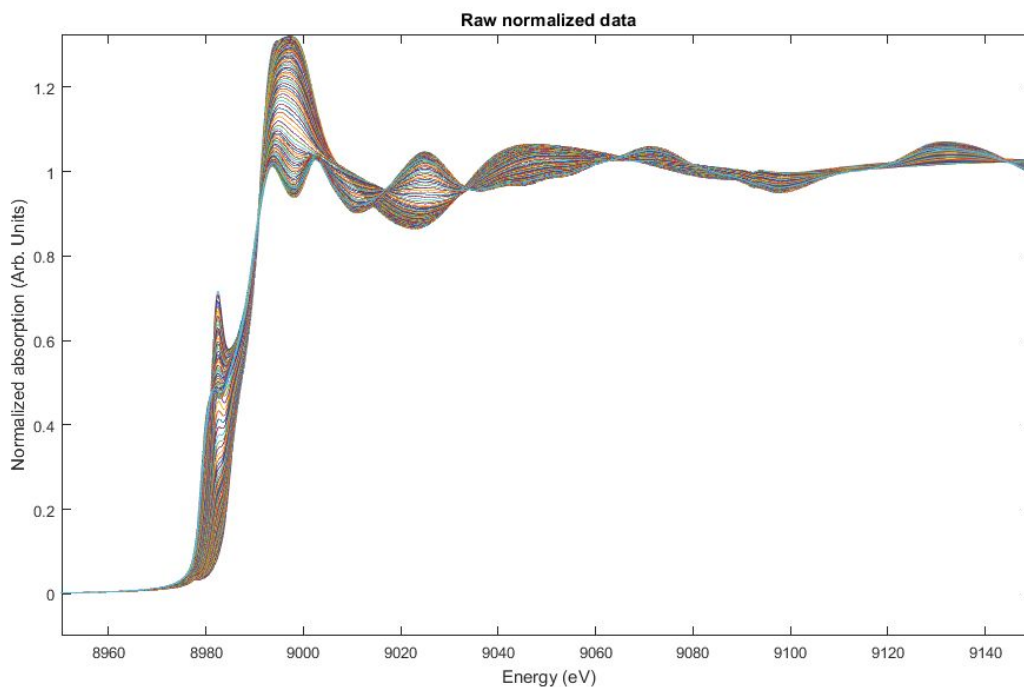

Figure 10.1: original dataset in a 2D representation of the Cu(hex)$_2$(HCOO)$_2$ complex. Every spectrum depicts another temperature during the in-situ heating profile. The spectral features of the Cu(II), Cu(I) and Cu(0) species can be clearly recognized.
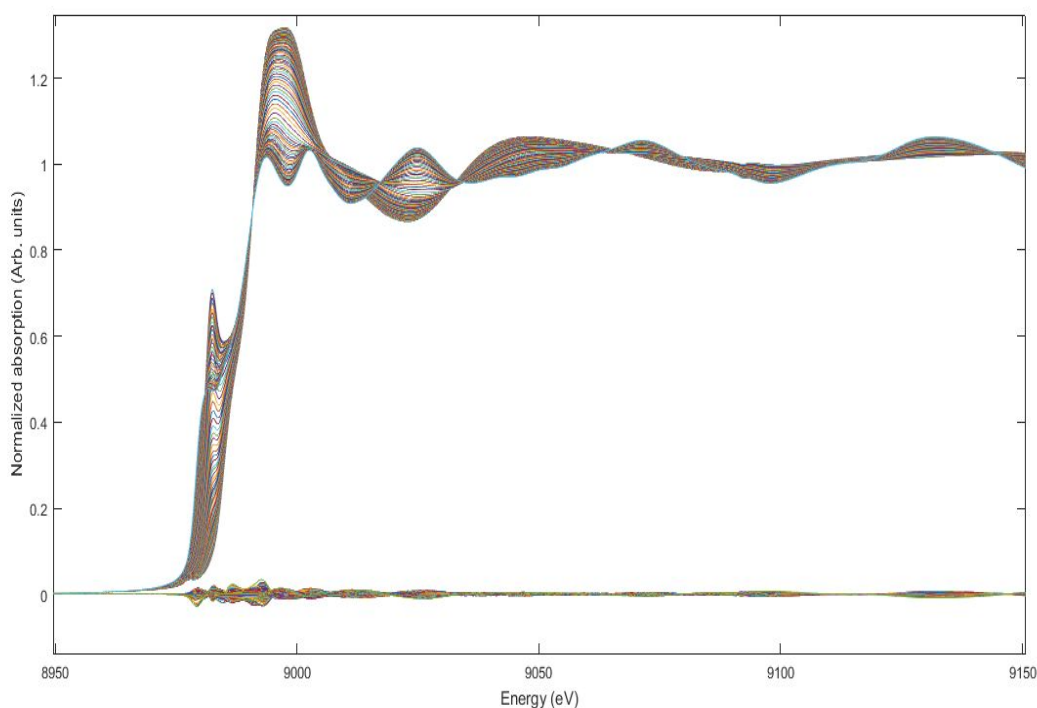
Figure S10.2: reconstructed dataset of the Cu(hex)$_2$(HCOO)$_2$ complex after matrix multiplication of the concentration profile and the pure spectra extracted by the MCR-ALS algorithm. In addition, the residuals representing the difference between the recorded and reconstructed spectra at every energy value are represented as well.

S 11: overview of the EXAFS fits on the Cu(I) intermediate complexes, performed on spectra isolated from the PCA-MCR-ALS algorithm, applied on the Cu(hex)$_2$(HCOO)$_2$ and Cu(etam)$_2$(HCOO)$_2$ dataset.

Table 11.1: overview of the fitted parameters for the Cu(hex)$_2$(HCOO) model structure. The table shows the degeneracy (N), distance (r), Debye-Waller factor (σ^2), a 95 % confidence interval for the distance based on r-E$_0$ shift mapping and the physical meaning of the shell. The fitted E$_0$ shift was found to be 8.38 eV.

Shell	Degeneracy	r fit	σ^2 fit	r 95% CI	Meaning
1	2	1.89	0.004	1.89 - 1.90	Cu-N, hexylamine, SS
2	1	2.36	0.007	2.34 - 2.38	Cu-O, formate, SS
3	2	2.69	0.011	2.67 - 2.70	Cu-C, hexylamine, SS
4	1	2.81	0.004	2.79 - 2.83	Cu-C, formate, SS
5	4	3.11	0.005	3.04 - 3.17	Cu-N-C, hexylamine, MS
6	2	3.64	0.003	3.51 - 3.74	Cu-N-N, hex, non-linear, MS
7	2	4.53	0.004	4.48 - 4.58	Cu-C-C, hex, non-linear, MS

Table 11.2: overview of the fitted parameters for the Cu(etam)$_2$(HCOO) model structure. The table shows the degeneracy (N), distance (r), Debye-Waller factor (σ^2), a 95 % confidence interval for the distance based on r-E$_0$ shift mapping and the physical meaning of the shell. The fitted E$_0$ shift was found to be 9.17 eV. The linear coordination can be confirmed due to the fact that the N-Cu-N and N-Cu-N-Cu multiple scattering pathways coincide.

Shell	Degeneracy	r fit	σ^2 fit	r 95 % CI	Meaning
1	2	1.92	0.005	1.90 - 1.94	Cu-N, ethanolamine, SS
2	1	2.69	0.003	2.67 - 2.71	Cu-O elongated, formate, SS
3	2	2.88	0.005	2.86 - 2.91	Cu-C, ethanolamine, SS
4	1	3.74	0.005	3.63 - 3.83	Cu-C, formate, SS
5	4	3.84	0.005	-	Cu-N-(Cu)-N, quasi-linear, ethanolamine, MS
6	2	4.21	0.007	4.11 - 4.31	Cu-C, ethanolamine, SS

S12: Multivariate Curve Regression with Alternating Least Squares Fitting Analysis of the Cu(pyr)$_2$(HCOO)$_2$ complex, showing the relative contribution of the 4 extracted distinct species and their corresponding spectra. The transition between both Cu(II) complexes is shown in a supplementary picture, illustrating the correspondence between the MCR-ALS and the macroscopically observed decomposition pathway.
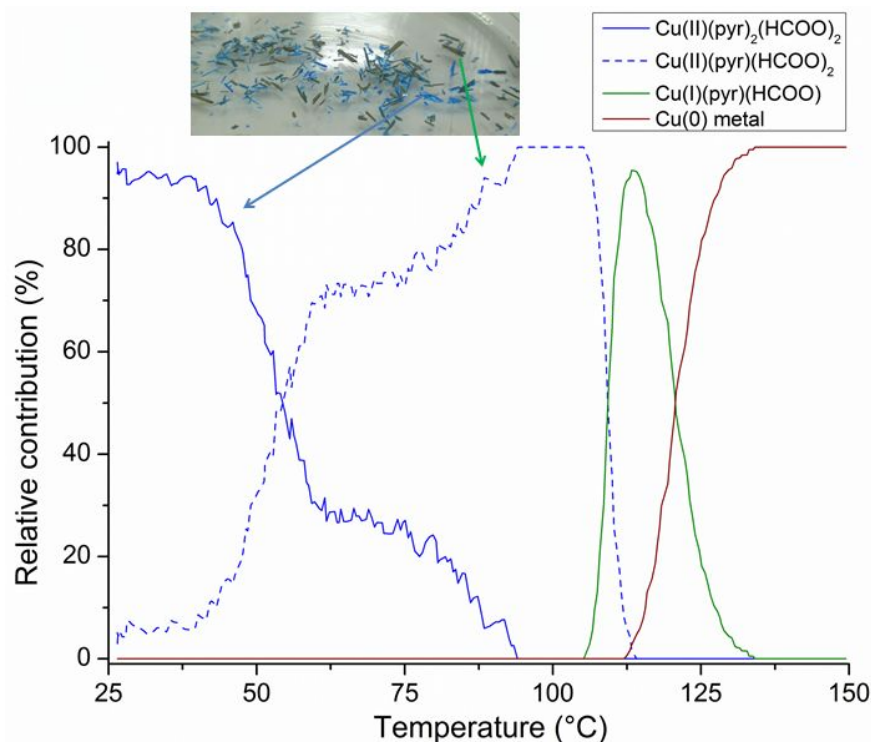

Figure S12.1: Relative contribution of the different Cu-species in the Cu(pyr)$_2$(HCOO)$_2$ decomposition. The profiles result from the MCR-ALS algorithm supported by PCA rank determination, applied on a data

matrix of approximately 700 spectra recorded from RT to 300 °C in an inert He atmosphere with a heating rate of 5 °C/min.
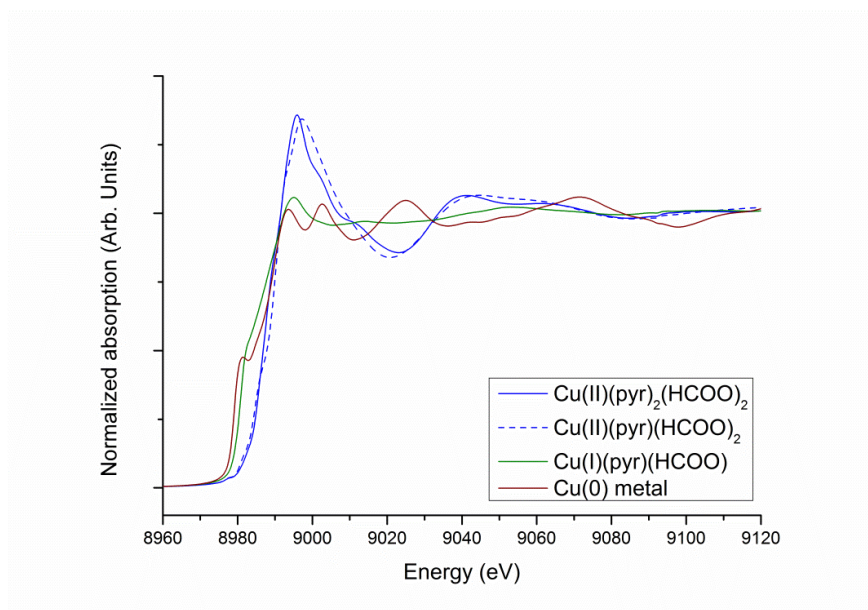

Figure S12.2: Overview of the different MCR-ALS extracted XANES spectra, depicted in the colors corresponding to the concentration profiles in figure S9.1. The spectra (in a broader energy range) can be processed further and fitted to a model compound (EXAFS). The model compounds and the results of the structure determination are shown in S11.

S13: TG-MS evolved gas analysis of the $Cu(pyr)_2(HCOO)_2$ MOD ink dried in vacuum (RT). The thermogram clearly indicates the loss of one pyridine ligand around 60 °C, and the m/z ion currents of the evolved gas correspond to pyridine (m/z = 79, 52, 51, 39,..). The Cu(II)→ Cu(I) →Cu(0) sequence is so fast that no separate CO_2 evolution steps (m/z = 44) could be detected in TG-MS. However, direct measurements on the copper complex clearly evidence the stepwise reduction.
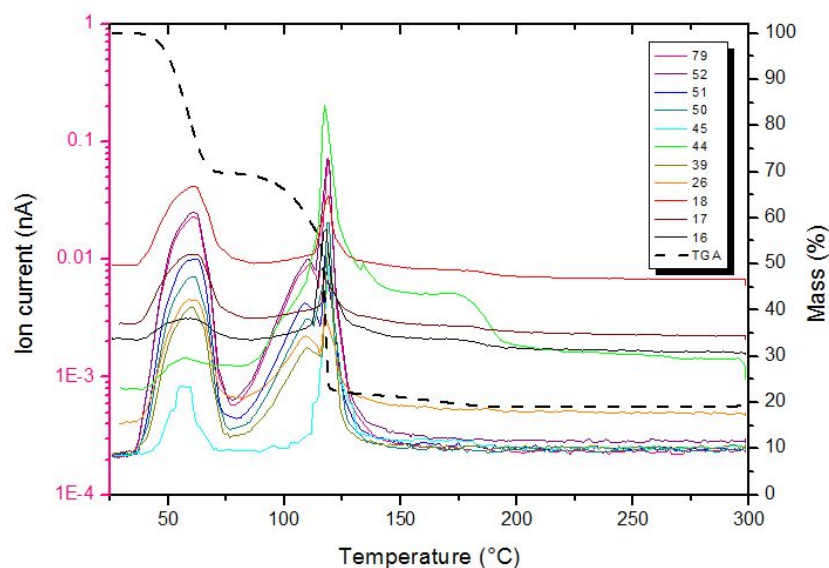
Figure S13: TG-MS measurement (N_2 atmosphere, 5°C/min heating rate) indicating the evolution of pyridine (50-75 °C), and the in-situ reduction (around 110-120 °C). The black dashed line is the corresponding thermogravimetric profile (right Y axis), whereas the ion current values (m/z of the ion fragments depicted in various colors, electron ionization) can be read out on the left axis.

S14: Structural determination of the intermediates appearing in the Cu(pyr)$_2$(HCOO)$_2$ *in-situ* reduction via EXAFS fitting on 'pure spectra' extracted from the data matrix after applying the MCR-ALS algorithm, supported by PCA rank determination.

shell	degeneracy	r fit	σ^2 fit	r 95 % CI	meaning
1	4	1.94	0.013	1.92 - 1.97	Cu-O, formate bridgers, SS
2	1	2.00	0.002	1.98 - 2.02	Cu-N, pyridine, SS
3	1	2.69	0.014	2.65 - 2.73	Cu-Cu, dimer, SS
4	4	2.80	0.040	constr.	Cu-C, formate bridgers, SS
5	2	2.95	0.010	2.87 - 3.04	Cu-C, pyridine ring, SS
6	8	3.02	0.005	2.94 - 3.09	Cu-O-C, formate bridgers, MS
7	4	3.32	0.031	3.18 - 3.44	Cu-O, other O's formate bridgers, SS
8	8	3.84	0.012	3.74 - 3.95	Cu-O-(Cu)-O, (small dihedral angle), SS
9	4	4.10	0.011	3.97 - 4.23	Cu-N-C, pyridine ring, SS

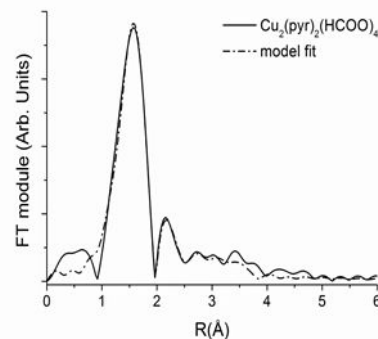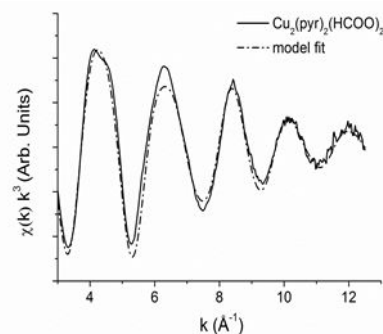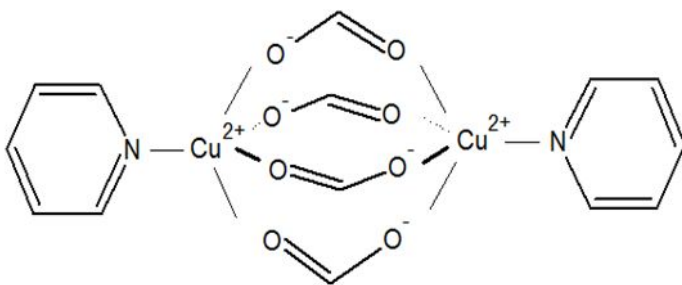*Figure S14.1: model structure and fitting parameters of the $Cu_2(pyr)_2(HCOO)_4$ dimer intermediate. The table shows the degeneracy (N), distance (r), Debye-Waller factor (σ^2), a 95 % confidence interval for the distance based on r-E_0 shift mapping and the physical meaning of the shell. The fitted E_0 shift was found to be 7.71 eV. The k-space and R-space fits are displayed on the right hand side and exhibit a lack of fit R^2 of 4.37 % and 2.40 % respectively, obeying the Nyquist criterion. Data were extracted after applying the PCA-MCR-ALS algorithms on the total spectrum matrix, showing the 'pure' Cu(II) intermediate component.*

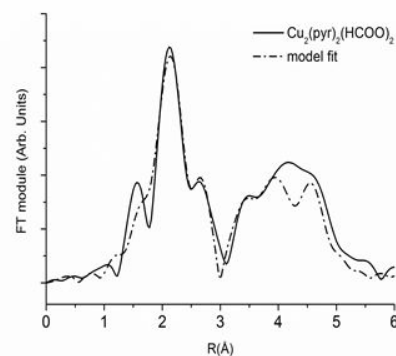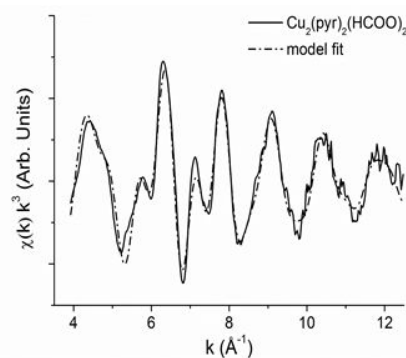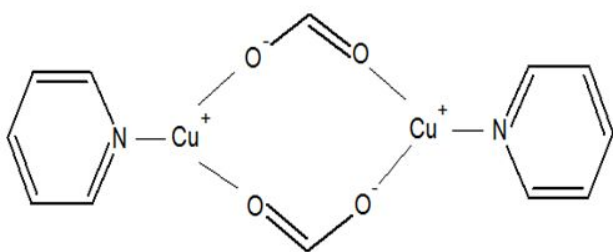| shell	degeneracy	r fit	σ^2 fit	error 95% CI	meaning
1	1	2.05	0.021	1.89 - 2.18	Cu-N pyridine, SS
2	2	2.57	0.007	2.54 - 2.60	Cu-O formate, SS
3	1	2.84	0.008	2.82 - 2.86	Cu-Cu dimeric unit, SS
4	2	3.02	0.005	-	Cu-C pyridine, SS
5	2	3.83	0.003	3.75 - 3.90	Cu-C formate, SS
6	2	4.04	0.015	3.98 - 4.10	Cu-Cu between stacked units, SS
7	4	4.38	0.005	-	Cu-O-N, MS
8	x = 7.99	5.11	0.008	5.03 - 5.18	Cu-Cu-x MS and pyridine ring MS

Figure S14.2: model structure and fitting parameters of the $Cu_2(pyr)_2(HCOO)_2$ dimer intermediate. The table shows the degeneracy (N), distance (r), Debye-Waller factor (σ^2), a 95 % confidence interval for the distance based on r-E_0 shift mapping and the physical meaning of the shell. The fitted E_0 shift was found to be 6.70 eV. The k-space and R-space fits are displayed on the right hand side and exhibit a lack of fit R^2 of 5.69 % and 4.12 % respectively, obeying the Nyquist criterion. Data were extracted after applying the PCA-MCR-ALS algorithms on the total spectrum matrix, showing the 'pure' Cu(I) intermediate component.

S15: PCA-MCR-ALS treated XAS spectra of the *in-situ* reduction mechanisms of Cu(en)$_2$(HCOO)$_2$ and the neat Cu(HCOO)$_2$ salt. In both cases, the Cu(I) intermediate appears to be very short living and unstable. Although MCR-ALS analysis clearly indicates the presence of a species with XANES features that cannot be explained by a simple superposition of the Cu(0) and Cu(II) edge, isolation of a pure Cu(I) spectrum remained impossible, even at lower heating rates of 2 °C/min (increasing the thermal resolution of the *in-situ* measurement). The presence of a Cu(I) species can be easily illustrated via linear combination analysis, showing a large residue in case no similar Cu(I) contribution is included in the edge reconstruction. The shown Cu(I) concentration profile at the top left side is a representation of the directly extracted MCR-ALS data, thus the relative contribution still needs to be corrected with a factor of approximately 0.45 to have an idea of the 'real Cu(I) contribution'.
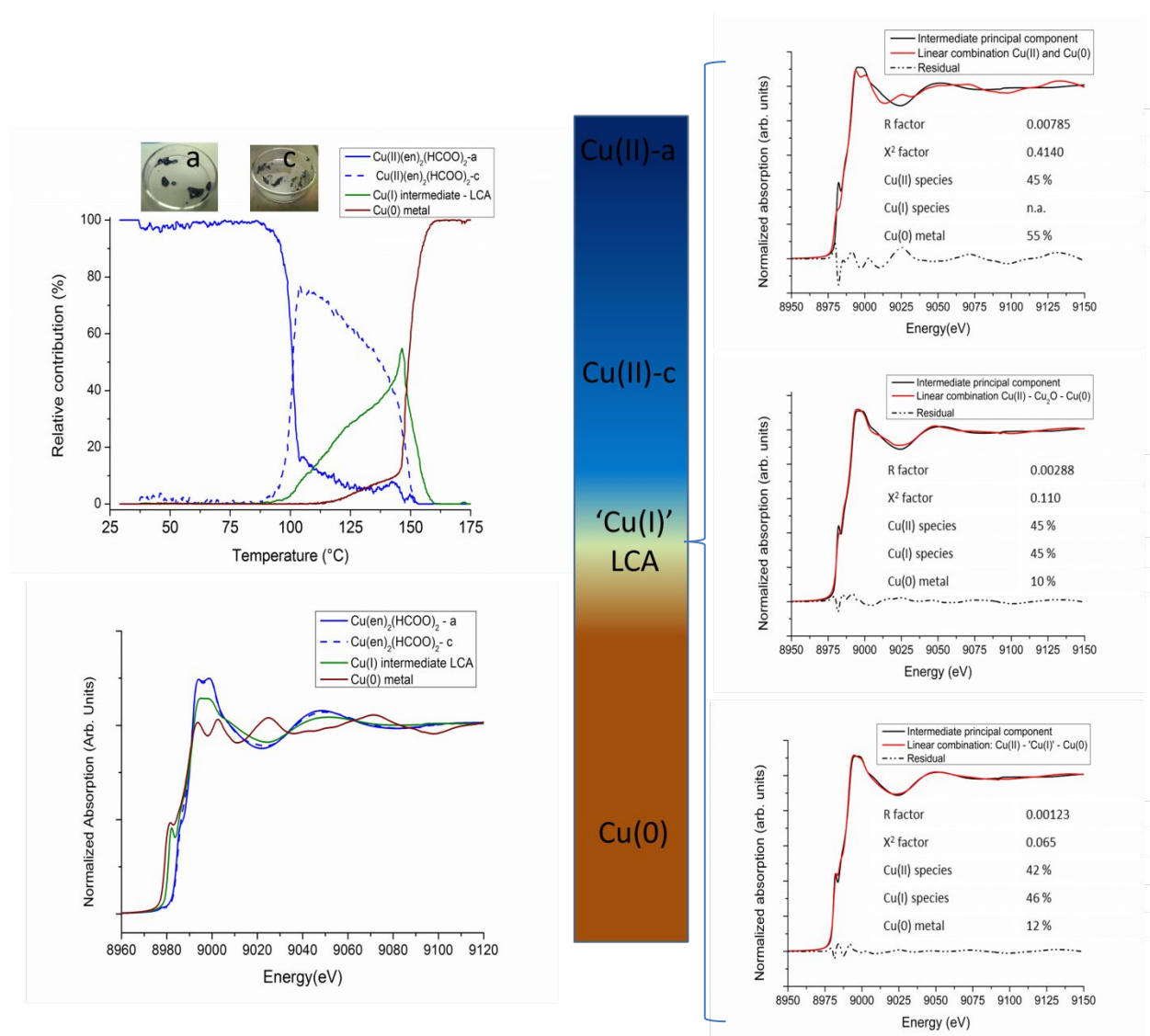
Figure S15.1: On the left hand side, the result of the MCR-ALS algorithm supported by PCA rank determination is presented, carried out on spectra for the Cu(en)$_2$(HCOO)$_2$ sample, heated with 2 °C/min in He atmosphere. On the right hand side, different linear combination analysis are demonstrated including no Cu(I) (top right), Cu$_2$O (middle right) or a Cu(I) hexylamine intermediate species (bottom right) in the fitting.

Further explanation figure S15.1: in the MCR-ALS analysis, a subtle difference between two Cu(II) species can be discovered, which can be linked to the crystallization of the Cu(en)$_2$(HCOO)$_2$ complex after removal of some residual ethanol. The transition can also be observed macroscopically (see pictures top left side of figure S15.1, labelled **a**morphous and **c**rystalline). Therefore, the labels a (amorphous) and c (crystalline) are assigned to the different Cu(II) spectra. Starting from 100 °C, a gradual transition to Cu(I) can be observed. Bear in mind that the lower heating rate shifts the apparent decomposition temperature. The edge structure is not clearly exhibiting distinct Cu(I) features. Therefore, an edge reconstruction as a linear combination of the present Cu(II) and Cu(0) species (top right hand side) was made. The poor agreement and the significant deviation between the LCA fit and the data (labeled as the residual), necessitates the inclusion of Cu(I) references for a superior edge reconstructions. This shows the presence of an unresolved Cu(I) transition. The LCA fits improves the more the included component in the LCA matches the assumed intermediate Cu(I) complex.
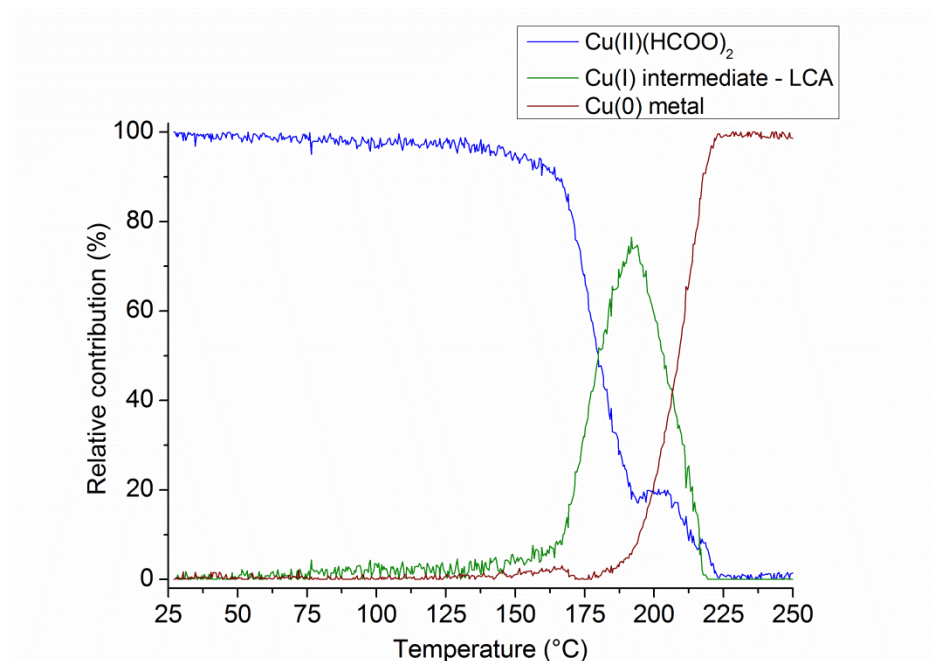

Figure S15.2: the relative concentration profiles during the Cu(HCOO)$_2$ decomposition, heated in He atmosphere with a 5 °C/min heating rate. Analysis at a lower heating rate (2 °C/min) did not prove new

insight or a better isolation of the Cu(I)species, which can also be considered as a superposition of Cu(II), Cu(I) and Cu(0) species in this case (see figure S15.3)
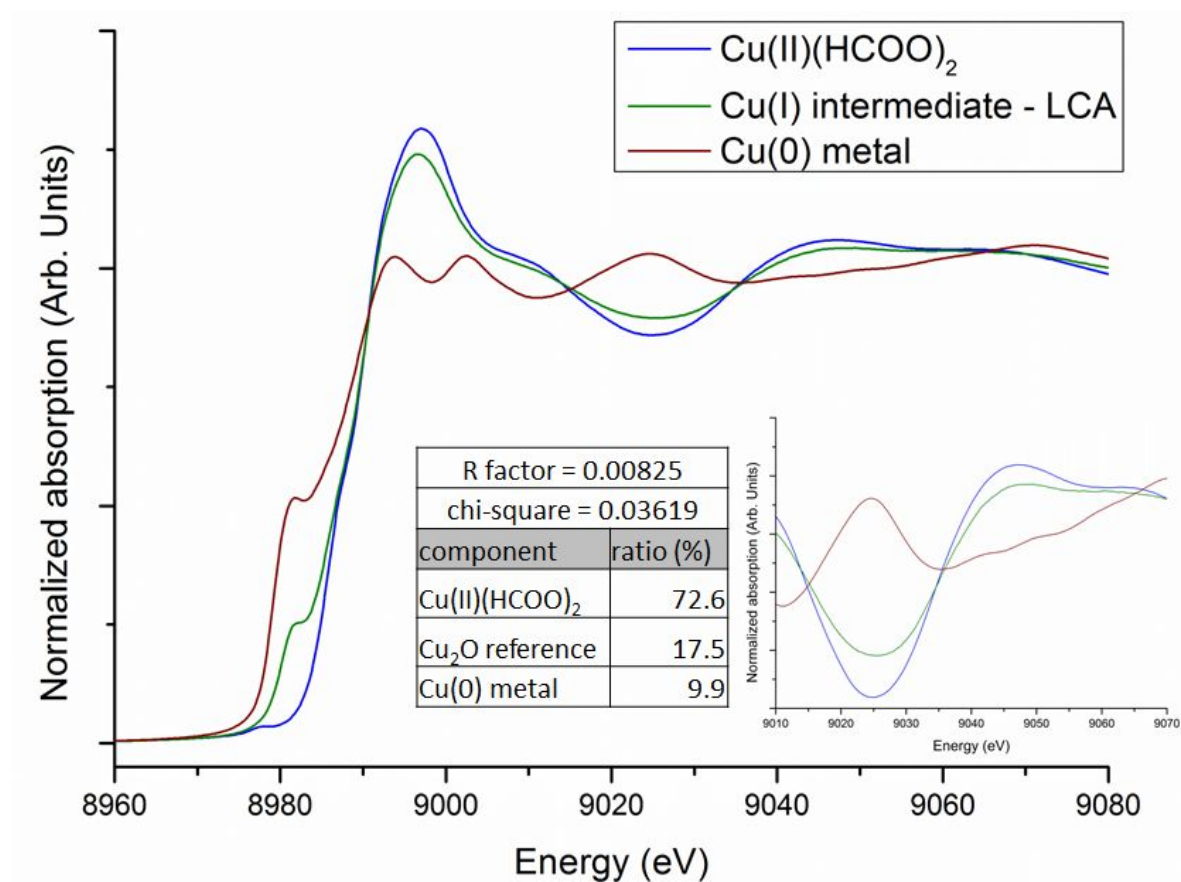

R factor = 0.00825	
chi-square = 0.03619	
component	ratio (%)
Cu(II)(HCOO)$_2$	72.6
Cu$_2$O reference	17.5
Cu(0) metal	9.9

Figure S15.3: overview of the MCR-ALS pure spectra corresponding to the concentration profiles in figure S15.2. The presence of at least 3 components can also be rationalized by the absence of isosbestic points (inset). The LCA analysis (details in figure S15.4) shows that approximately 17.5 % of the MCR-ALS generated intermediate XAS spectrum consists out of a Cu(I) species.
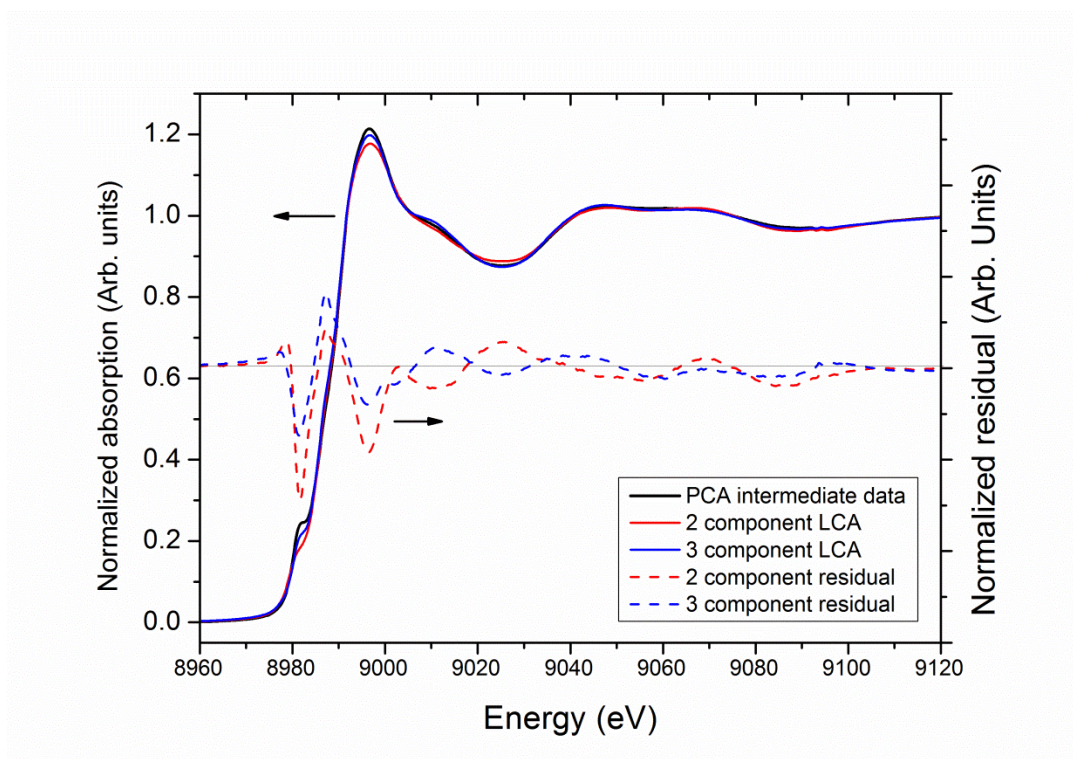
Figure S15.4: Linear combination analysis on the Cu(I) intermediate shown in figure S15.3.It can be clearly observed that inclusion of a Cu(I) reference (like Cu_2O in this case) improves the closeness of fit and the XANES reconstruction (3 component LCA), compared to a superposition of only the present Cu(II) and Cu(0) species (2 component LCA).

S16: TG-MS evolved gas analysis of the Cu(en)$_2$(HCOO)$_2$ MOD ink dried at 80 °C and in vacuum (RT). The *in-situ* reduction occurs at a relatively high temperature compared to the other studied amine-complexes, but proceeds swiftly once initiated and no separate CO$_2$ peaks can be resolved (m/z = 44). The onset and peak maximum of the mass fragments related to ethylene diamine are shifted to higher temperatures (electron ionization: m/z = 43, 41, 30, 27, ...), suggesting that ethylene diamine only evolves after the Cu(II)→Cu(I) conversion, imposing a square planar Cu(I) coordination geometry, which matches the general reasoning in this study.
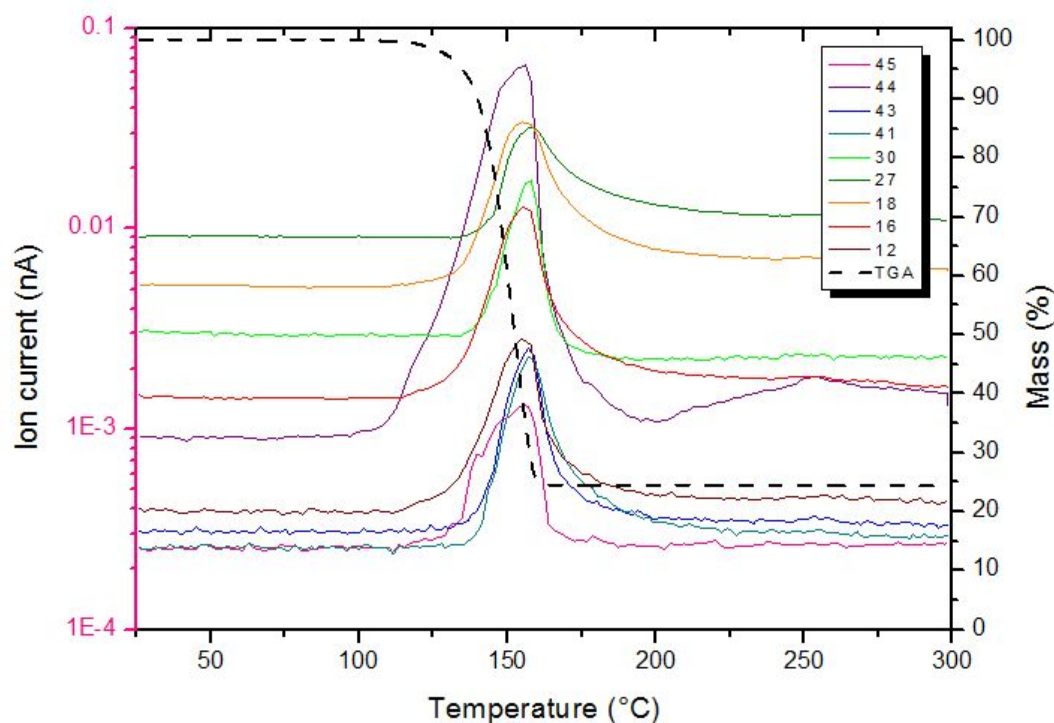

Figure S16: TG-MS measurement (N$_2$ atmosphere, 5°C/min heating rate) showing the in-situ reduction starting around 145 °C. The black dashed line is the corresponding thermogravimetric profile (right Y axis), whereas the ion current values for the different m/z fragments (electron ionization) can be read out on the left axis.

S17: Decomposing the drop-casted copper MOD inks in inert atmosphere on different PET substrates results in metallic copper deposition. For this purpose, inks which show an *in-situ* reduction under 150 °C are selected not to thermally deform/ destroy the PET substrates.
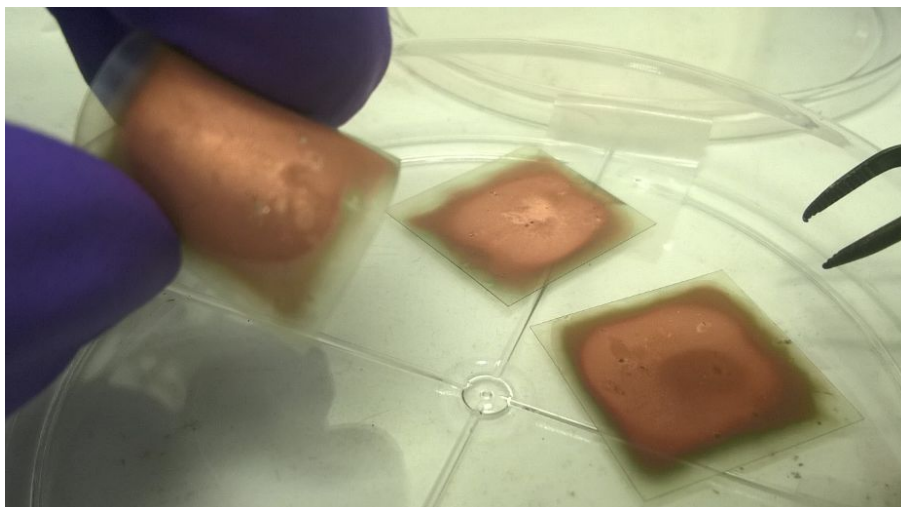
Figure S17: Cu(hex)$_2$(HCOO)$_2$ drop casted inks on PET foil, treated in vacuum using a heating program ramping from room temperature up to 150 °C, with a 10 minutes isothermal period.

S18: TGA measurements on different nickel-formate based complexes in which similar amines are used for coordination. The compositions of the complexes were checked *via* CHN analysis. Ni(H$_2$O)$_2$(HCOO)$_2$ was bought from Sigma-Aldrich and used as received.
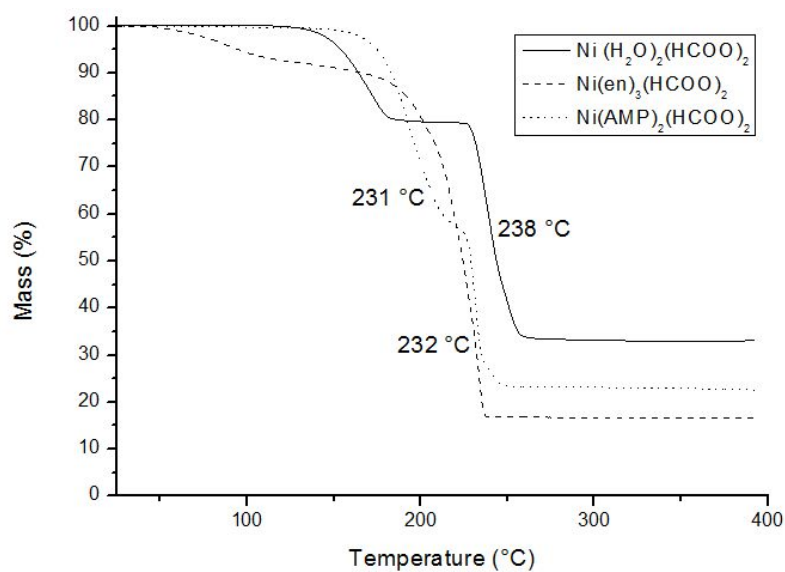

Figure S18: TGA profiles of the related Ni coordination compounds, together with a displayed value for the DTG maxima of the last decomposition step (200-250 °C) which represents the in-situ reduction.

Supplementary references

1.   Stern, E.A. Number of relevant independent points in x-ray-absorption fine-structure spectra. *Physical Review B* **1993**, *48*, 9825-9827.
2.   Frenkel, A.I.; Korshin, G.V.; Ankudinov, A.L. Xanes study of Cu2+-binding sites in aquatic humic substances. *Environmental Science and Technology* **2000**, *34*, 2138-2142.